frontiers | Frontiers in Earth Science

TYPE Original Research
PUBLISHED 07 October 2024
DOI 10.3389/feart.2024.1470723

OPEN ACCESS

EDITED BY
Hongjian Zhu,
Yanshan University, China

REVIEWED BY
Shiming Wei,
China University of Petroleum, China
Wenda Li,
Taiyuan University of Technology, China
Mengke An,
Hong Kong Polytechnic University, Hong Kong SAR, China

*CORRESPONDENCE
Xingchuan Liao,
liaoxc1998@163.com

RECEIVED 26 July 2024
ACCEPTED 09 September 2024
PUBLISHED 07 October 2024

CITATION
Du F, Liang B, Ren Y, Liao X, Pei L, Fan Z and Liu W (2024) Study on failure mechanism of cracked coal rock and law of gas migration. *Front. Earth Sci.* 12:1470723. doi: 10.3389/feart.2024.1470723

Study on failure mechanism of cracked coal rock and law of gas migration

Feng Du[1,2,3], Bing Liang[4], Yixing Ren[5], Xingchuan Liao[5]*, Lingjun Pei[5], Zuoyuan Fan[6] and Wei Liu[7]

[1]College of Mining, Liaoning Technical University, Fuxin, China, [2]China Coal Technology and Engineering Group Shenyang Research Institute, Fushun, China, [3]State Key Laboratory of Coal Mine Safety Technology, Fushun, China, [4]School of Mechanics and Engineering, Liaoning Technical University, Fuxin, China, [5]School of Civil Engineering and Geomatics, Southwest Petroleum University, Chengdu, Sichuan, China, [6]School of New Energy and Materials, Southwest Petroleum University, Chengdu, Sichuan, China, [7]Development Department, PetroChina Southwest Oil and Gasfield Company, Chengdu, China

China possesses abundant coal resources and has extensive potential for exploitation. Nevertheless, the coal rock exhibits low strength, and the coal seam fractures due to mining activities, leading to an increased rate of gas emission from the coal seam. This poses significant obstacles to the exploration and development of the coal seam. This paper focuses on studying the failure mechanism of fractured coal rock by conducting uniaxial and triaxial compression experiments on the coal rock found at the Wangpo coal mine site. Simultaneously, in conjunction with the findings from the field experiment, a gas migration model of the mining fracture field is constructed to elucidate the pattern of coal seam gas distribution during mining-induced disturbances. The study structure reveals that coal rock exhibits three distinct failure modes: tensile failure, shear failure, and tension-shear failure. The intricate fissure in the rock layer will intensify the unpredictability of rock collapse patterns. The compressive strength of coal rock diminishes as the confining pressure drops. The coal rock in the working face area will collapse as a result of the lack of confining pressure. In the rock strata above the mining fracture zone, the gas pressure is first higher and then significantly falls with time. After 100 days of ventilation, the low gas pressure area changes little, so to ensure the safety of the project, the ventilation time of the fully mechanized mining surface is at least 100 days. The research results will help to establish the core technology system of coal seam development and improve the competitiveness of coal seam resources in China.

KEYWORDS

physical experiment, failure mechanism, gas migration, coal rock, numerical simulation

1 Introduction

As economic globalization intensifies and scientific and technological progress advances rapidly, the energy demand in all countries is growing on a daily basis (Chi et al., 2024; Huang et al., 2019; Gao et al., 2023; Cui et al., 2024; Huang et al., 2024; Zhu et al., 2021; Huang et al., 2023a; Zhu et al., 2018; Zhang F. et al., 2022; Huang et al., 2022; Tan et al., 2024a). As the world's

largest developing country, China is facing huge energy challenges in economic development (Zheng et al., 2022; He et al., 2023; Gao et al., 2023; Huang et al., 2023b; Luo et al., 2022; Zhou et al., 2023; Huang et al., 2020; Fu et al., 2024). Due to China's huge coal reserves and limited reserves of oil and natural gas, coal has historically served as the main source of energy consumption, accounting for about 70% of annual energy consumption (Li Y. et al., 2022; Chen et al., 2022a; Li D. et al., 2018; Wang et al., 2013; Tao et al., 2022; Tan et al., 2024b). While the transition to a new economic growth model and the enforcement of energy conservation and emission reduction legislation may limit the expansion of the coal sector, it still holds the potential for long-term sustainable growth (Chen J. et al., 2022; Yuan, 2018; Chen et al., 2022c; Li and Hu, 2017; Wang and Cao, 2022). Coal mining has formed a complete working system (Zhang Q. et al., 2022; Saber et al., 2024; Chen and Xu, 2010; Wang et al., 2012). Nevertheless, due to the impact of mining activity, the distortion and destruction of the coal seam on the working face intensify the rate at which coal seam gas is emitted, posing challenges in properly managing construction safety at the site (Fu et al., 2020; Kuang et al., 2023; Wang et al., 2020). Therefore, effectively predicting and controlling coal seam gas concentration is still a significant problem that needs to be solved.

When mining disrupts the coal seam, it disrupts the original balance of stress and causes the stress distribution in the coal seam and rock strata to be redistributed (Liu et al., 2022a; Chai et al., 2023; Zhang et al., 2024; Yang et al., 2023a; Jia et al., 2022). In front of the advancing of the working face, the supporting pressure will be formed, while above the goaf, the overlying strata will sink to different degrees due to the loss of support, creating the fracture field caused by mining (Tian et al., 2020; Li S. et al., 2018). The strength of coal rock will drastically decrease as a result of reduced confining pressure. This typically leads to engineering issues, such as the collapse of the working face, hence increasing the safety risk during site development (Xiong et al., 2022; Liu et al., 2022b; Kong et al., 2019). To accurately understand the influence of stress changes on the strength properties of coal rock, yang et al. used uniaxial compression experiments to point out four stages of coal rock failure: crack compaction closure, elastic deformation, crack expansion, and stress reduction (Yang et al., 2023b). Song et al. explored the mechanical properties of coal rock under the disturbance of coal seam excavation by using the cyclic loading method in uniaxial compression. They pointed out that uniaxial compressive strength, elastic modulus, and anisotropic Angle (0–90°) are usually U-shaped. At the same time, the peak strain is characterized by first decreasing and then increasing, and the minimum and maximum values are obtained at the anisotropic angles of 22.5° and 90°, respectively (Song et al., 2024). Zhang et al. used a thermal-fluid-solid coupling triaxial servo seepage experiment device to conduct mechanical and permeability experiments on gas-bearing raw coal samples under conventional triaxial compression, and the research shows that the peak strength of gas-bearing coal increases linearly with the increase of confining pressure (Zhang et al., 2021). Jia et al. adopted AE and triaxial compression experiments to understand the damage evolution law of coal rocks with different buried depths (Jia et al., 2020). They pointed out that under the influence of confining pressure caused by increasing ground stress, the AE activity and average crack size of coal seam decrease with increasing depth. The deeper the coal seam, the more small cracks and the greater the plastic strain.

With the continuous advance of the working face, the distribution of abutment pressure in front of the working face and the mining-induced fracture field above the goaf will experience space-time evolution (Cheng et al., 2020; Liu C. et al., 2022; Jiang et al., 2024; Liang et al., 2018). This evolution process will lead to changes in the structure of the coal seam and then promote the desorption of the gas adsorbed in the coal seam into free gas (Cui and Bustin, 2005; Alexeev et al., 2007). This change further affects the gas migration law in the mining fracture field in front of the working face and above the goaf, making the gas concentration in the field often exceed the expected level (Wang et al., 2023; Shu et al., 2022). Qin et al. put forward a free gas density gradient (FGDG) theoretical model and established a mathematical model of gas desorption flow in a coal matrix based on this model, providing a method to explain gas transport in the coal matrix on the whole time and pressure scale (Qin et al., 2020). Gan et al. established a multi-mechanism diffusion-seepage model of gas in micro-nanopores of coal. They pointed out that when pore pressure is greater than 3.5MPa, apparent permeability decreases first and then increases with the increase of pore radius (Gan et al., 2024). Zeng et al., using research methods based on desorption theory and elastoplastic mechanics, established a gas transport model around coal micro-fissures that considered dynamic microfissure width changes and effective gas viscosity (Zeng et al., 2019). The research shows that coal microfissure permeability positively correlates with rock mechanics parameters (Young's modulus and Poisson's ratio) and negatively correlates with fracture compression. However, the above research did not consider the structural changes of coal seams caused by mining disturbance, and the results obtained have obvious shortcomings.

This paper focuses on studying the mechanical strength changes of coal rock at the Wangpo coal mine site. The research is conducted through uniaxial and triaxial compression tests. The paper thoroughly examines the impact of these changes on the driving face and fully mechanized mining face. Additionally, it uncovers the typical characteristics of *in-situ* coal rock failure, and the mechanism of coal rock damage under mining disturbance has been clarified. Furthermore, by integrating the field detection data, we develop a gas migration model for the mining fracture field and conduct a detailed analysis of the distribution pattern of coal seam gas under stress disturbance, as shown in Figure 1. The research findings will offer essential theoretical backing and technical direction for on-site coal seam mining.

2 Experimental methods and instruments

A microcomputer-controlled electro-hydraulic servo universal experimental machine is used in this experiment to study the stress-strain characteristics of coal rock under uniaxial compression, as shown in Figure 2A. The instrument can apply a maximum pressure of 600 kN while offering high sensor accuracy with an overall error rate of ±0.5%. The test uses the standard sample with ϕ 25 × 50 mm, and the loading rate is set to 0.1 mm/min. Significant disparities in rock mechanical strength often arise because of

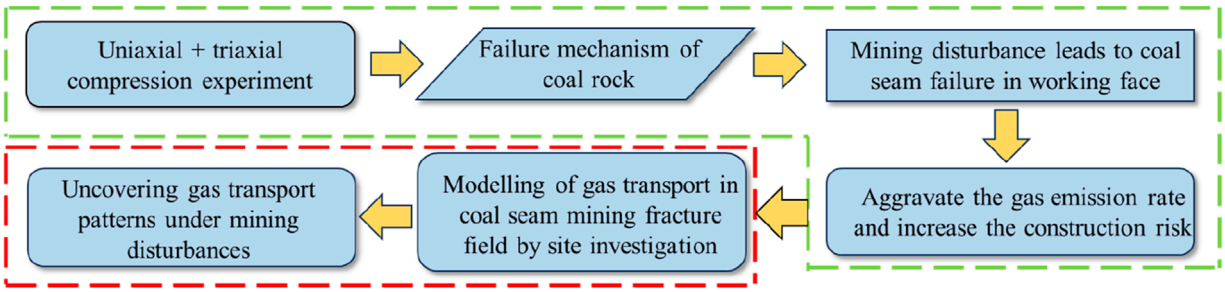

FIGURE 1
Research idea. The green box lines represent physical tests, whereas the red box lines represent numerical models.

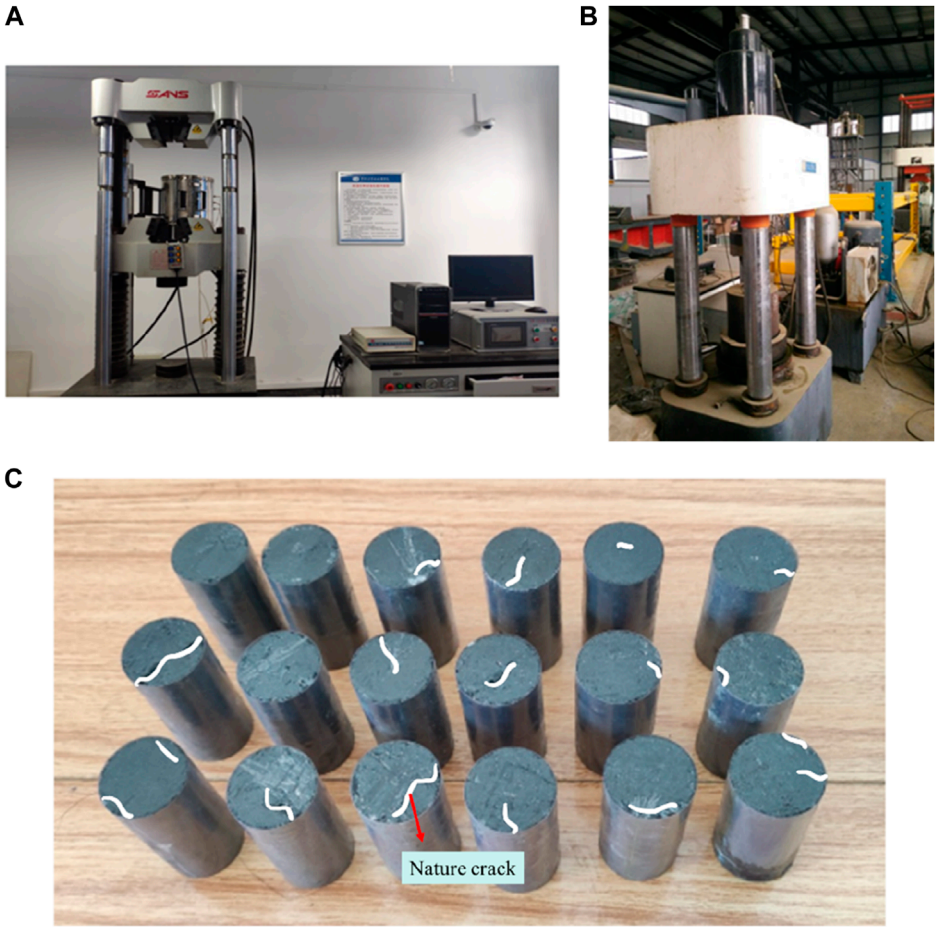

FIGURE 2
Experimental equipment and schematic diagram of coal rock samples. **(A)** Microcomputer controlled electro-hydraulic servo universal experimental machine; **(B)** Microcomputer servo rock triaxial testing machine; **(C)** coal rock samples. The microcomputer controlled electro-hydraulic servo universal experimental machine can apply a maximum pressure of 600 kN while offering high sensor accuracy with an overall error rate of ±0.5%. The test uses the standard sample with ϕ 25 × 50 mm, and the loading rate is set to 0.1 mm/min. The microcomputer servo rock triaxial testing machine can achieve the maximum axial stress of 600 kN, the axial displacement of 10 mm, and the test accuracy of up to ±1%. The sample contains a significant abundance of primary natural fractures.

variations in the nature of coal rock between the driving face and the fully mechanized mining face. Hence, this experiment has six groups, with three of them being assigned to the driving and fully mechanized mining faces.

In addition, to effectively reduce the mechanical strength index of coal rock under a triaxial stress state, this paper carried out a triaxial compression test relying on the microcomputer servo rock triaxial testing machine. The test equipment is shown in

TABLE 1 Test plan.

Confining pressure (MPa)	Number of samples (pieces)	Loading mode
0	3	Stress control
2	3	Stress control
4	3	Stress control
6	3	Stress control
8	3	Stress control
10	3	Stress control

Figure 2B. The device can achieve the maximum axial stress of 600 kN, the axial displacement of 10 mm, and the test accuracy of up to ±1%. The specific test scheme is shown in Table 1. The confining pressures of the tests were 0 MPa, 2 MPa, 4 MPa, 8 MPa, and 10 MPa, respectively. Each group of tests contained three coal samples, which were loaded by stress control until the residual strength of the coal samples remained stable. As shown in Figure 2C, natural cracks in coal rock samples are relatively developed.

3 Experimental result

3.1 Uniaxial compression experiment

The stress-strain under uniaxial compression test is shown in Figure 3, in which Figures 3A–C are the test results of fully mechanized mining face, and Figures 3D, E are the test results of driving face. The test results show that the uniaxial compression curve can be divided into four stages: compaction stage, elastic stage, yield stage, and failure stage. At the initial stage, with the increase of load, the sample's internal pores and structural planes are gradually compacted. The curve then rises rapidly into the elastic stage, in which the specimen is compacted. The curve enters the yield stage with the continuous load increase, and a slight disturbance occurs. At this time, the deformation of the sample begins to change from axial compression to transverse expansion, accompanied by a small crack. When the peak stress is reached, the failure stage is entered. Currently, macroscopic cracks appear on the specimen surface, and the internal stress field is rearranged.

The failure mode of the sample is shown in Figure 4. During loading, two prominent shear cracks first appeared at the bottom of the sample J-1. With the increase of load, the cracks were connected and then extended in the form of tensile failure, and finally, a "Y" shaped crack is formed, accompanied by micro-cracks and detachment phenomenon. Two tension cracks appeared on the upper end of sample J-2, which extended downward and caused the destruction of the upper end. Later, the cracks penetrated through the whole sample, and the middle part fell off. Sample J-3 shows shear failure. When loading, shear cracks appear at the top and middle of the sample at the same time, and cracks penetrate the sample to form an "X"shaped crack.

The shear crack first appeared at the upper end of sample Z-1 and gradually extended downward. When the crack developed to the middle of the sample, it intersected with the natural crack inside to form a macro crack, which ran through the whole sample. The shear crack at the upper end is deflected after passing through the natural crack and becomes a tension crack after extending for some distance. The failure mode of specimen Z-2 is a shear failure. Three shear cracks appear at the upper end and extend downward. The left two shear cracks are connected, forming a single shear crack to continue to extend. The two cracks intersect in the middle of the sample and run through the whole sample, and the cracks show a "Y"shape expansion. The shear failure of specimen Z-3 is also observed. The shear crack at the upper end intersects with the natural crack. It extends along the direction parallel to the specimen's top surface, resulting in the spalling of the specimen.

The experimental data is shown in Table 2. Due to the existence of many uncontrollable factors in the physical experiment and the difference in the internal structure of coal rock, there is a large gap between some experimental data, so the average value of similar ones is selected as the final experimental results. In other words, coal rock's compressive strength and elastic modulus on the excavation face are 5.464 MPa and 0.652. The compressive strength of coal rock at a fully mechanized mining face is 20.196 MPa, and the elastic modulus is 1.277.

3.2 Triaxial compression experiment

3.2.1 Situation in confining pressure of 0 MPa

Under the condition of confining pressure of 0 MPa, the stress-strain curve is shown in Figure 5. It can be seen that the stress-strain curves of the three coal rock samples show significant differences. This difference is mainly due to the different degrees of development of natural cracks in coal samples. Therefore, the stress-strain behavior of each sample is different in the compaction, damage, and failure stages during the test.

The stress-strain curve especially shows large fluctuations in the later stages of the test in Figure 5C. This fluctuation is probably due to the effect of cracks in the coal rock when subjected to pressure. When pressure acts on coal rock, the expansion and closure of internal cracks will lead to the fluctuation of stress and strain.

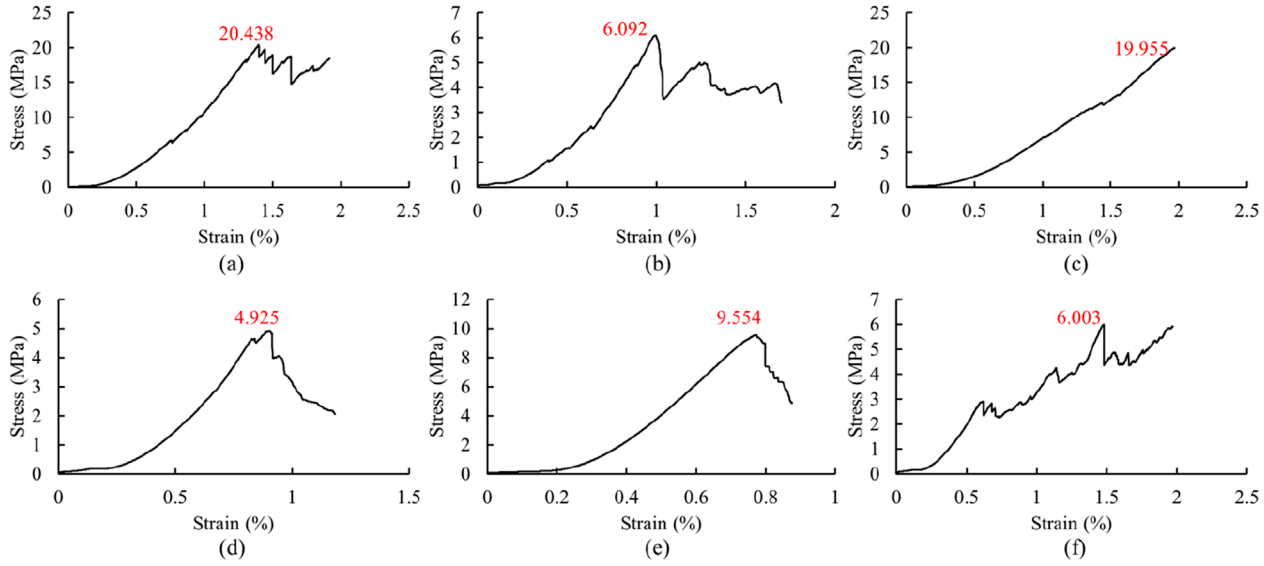

FIGURE 3
Stress-strain curve of uniaxial compression. **(A)** Z-1, **(B)** Z-2, **(C)** Z-3, **(D)** J-1, **(E)** J-2, **(F)** J-3. Where Z stands for fully mechanized mining face, and J stands for driving face.

The failure form of the specimen in the test is shown in Figure 6. In the process of stress loading, a large number of cracks were produced at the top and bottom of the specimen. A typical shear crack is extended through the specimen in the middle of the specimen. These cracks eventually form a fracture network that connects the specimen to develop natural cracks, resulting in a complete fracture of the specimen. This failure mode further confirms the critical influence of internal fractures on specimens' stress-strain properties and failure forms.

3.2.2 Situation in confining pressure of 2 MPa

Figure 7 shows the stress-strain curve of the sample under the confining pressure of 2 MPa. Compared with the stress-strain diagrams of the three samples when the confining pressure is 0 MPa, it can be observed that the ultimate compressive strength of the samples increases with the increase of the confining pressure. In Figure 7C, the stress at the end of the curve remains at a certain level after it has been reduced for a certain distance and does not continue to decrease. The characteristics of coal rock specimens often cause this phenomenon. Even if the specimen is damaged, it still has a specific residual strength inside, so the stress-strain curve shows a plateau after the decline.

When the confining pressure is 2 MPa, the compressive strength of the specimen is generally higher than that when the confining pressure is 0 MPa. The degree of breakage of the specimen is also more apparent. As shown in Figure 8, under the combined action of axial pressure and confining pressure, the specimen produces long shear cracks, which run through the top of the specimen, resulting in noticeable pressure loss on the top of the specimen, and the appearance of pulverized coal cinder. In addition, the previously formed shear cracks extend to the top and bottom of the specimen, connecting with the natural cracks that exist in the middle of the specimen. Despite this, the integrity of the specimen is maintained and not destroyed.

3.2.3 Situation at a confining pressure of 4 MPa

With the gradual increase of confining pressure, the peak stress of coal rock failure also shows an upward trend, while the ultimate strain of the specimen remains relatively stable. In this test, the natural fracture content of the three specimens selected is relatively low, so their stress-strain curves do not show significant fluctuation characteristics, as shown in Figure 9. The failure mode of the specimen is shown in Figure 10, which is mainly manifested as top collapse, and a large number of shear failure cracks and tensile failure cracks appear in the middle of the specimen. This phenomenon shows that the natural cracks in the specimen are gradually compressed when pressure is applied. It is worth noting that the specimen was not immediately destroyed due to confining pressure. Still, after the shear cracks are generated, these cracks gradually expand and connect and eventually extend to the stressed area. Therefore, despite the existence of cracks on the surface of the specimen, the ultimate compressive strength of the specimen under the action of confining pressure is increased compared with that under the confining pressure of 0 MPa.

3.2.4 Situation in confining pressure of 6 MPa

When the confining pressure is 6 MPa, the ultimate compressive strength of the three coal specimens in this group presents significant differences, and the stress-strain curves of each specimen have obvious fluctuations, as shown in Figure 11. This phenomenon indicates a large number of natural cracks in the specimen. Although the confining pressure was increased compared with the previous tests, the specimens' ultimate compressive strength remained low. As shown in Figure 11B, the stress-strain curve shows a second prominent rise at the end, which means the natural cracks developed

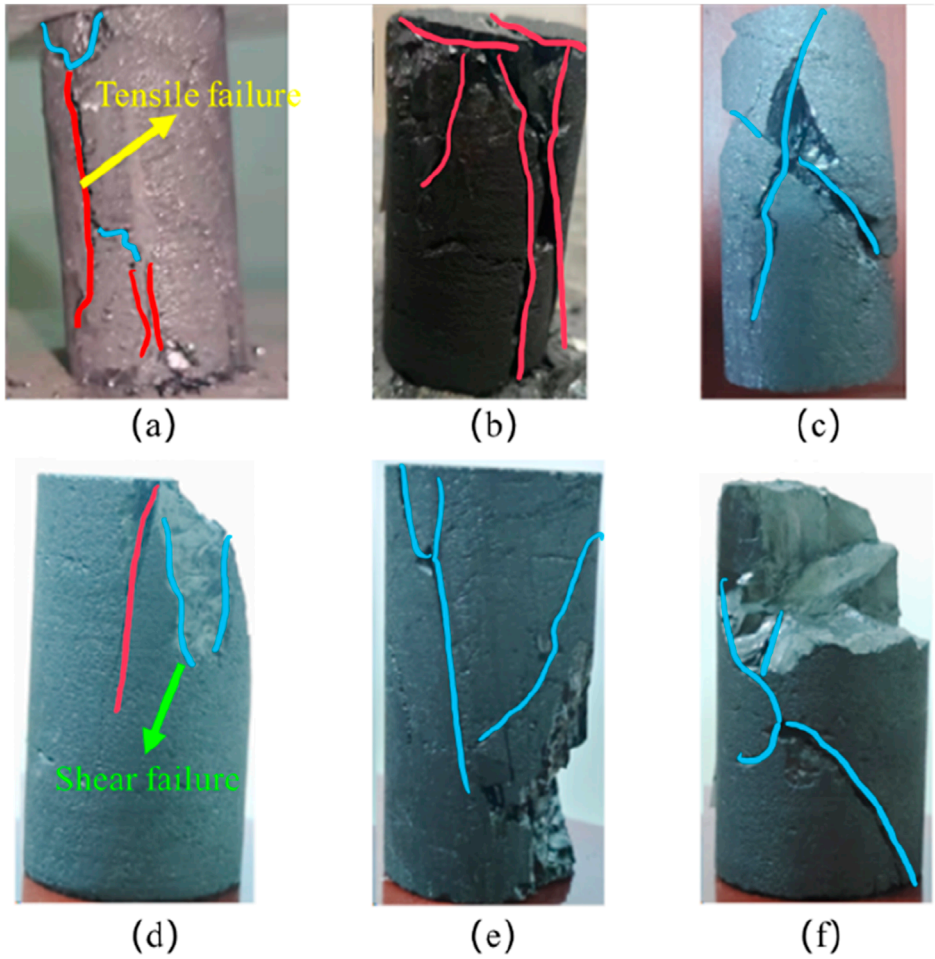

FIGURE 4
Failure modes of uniaxial compression of coal rock (Blue shear failure, red tensile failure). **(A)** J-1; **(B)** J-2; **(C)** J-3; **(D)** Z-1; **(E)** Z-2; **(F)** Z-3. Tensile failure and shear failure are both present in coal rock failure. Due to the large number of natural cracks in the samples, the final damage degree of the samples varies greatly.

TABLE 2 Results of mechanical parameters of samples.

Code	Compressive strength (MPa)	Average compressive strength (MPa)	Modulus of elasticity (GPa)	Average modulus of elasticity (GPa)
J-1	4.925	5.464	0.774	0.652
J-2	9.554		1.74	
J-3	6.003		0.53	
Z-1	20.438	20.196	1.71	1.485
Z-2	6.092		0.86	
Z-3	19.955		1.26	

inside the specimen significantly increase the randomness of the strength. Figure 12 shows the typical failure mode of this group of specimens under high pressure: the shear-tension mixed failure. The shear crack and the tension crack extend to the specimen's edge, causing the specimen's top and bottom to break and finally causing the specimen to fail.

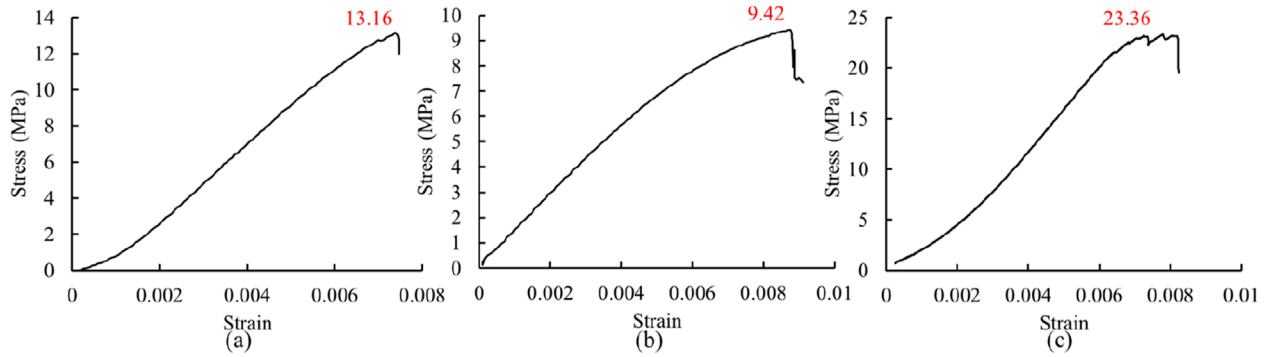

FIGURE 5
Stress-strain curve at confining pressure of 0 MPa. **(A)** 1; **(B)** 2; **(C)** 3. The enrichment of natural cracks in coal rock samples leads to a high degree of difference in experimental results.

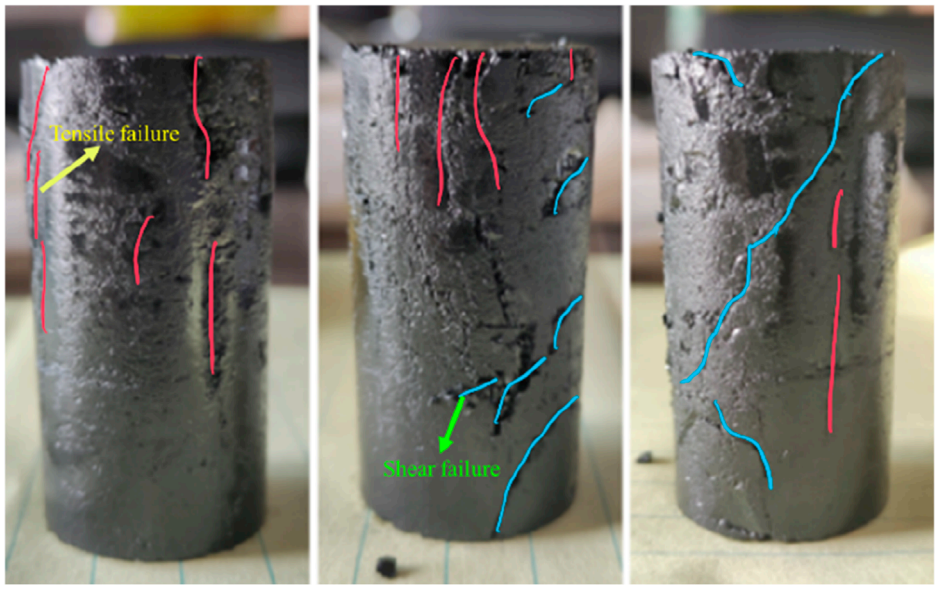

FIGURE 6
Schematic diagram of typical failure forms of specimens at confining pressure of 0 MPa (Blue shear failure, red tensile failure). During the test, the coal rock undergoes fracture starting from both ends of the sample and then develops shear cracks in the middle of the sample.

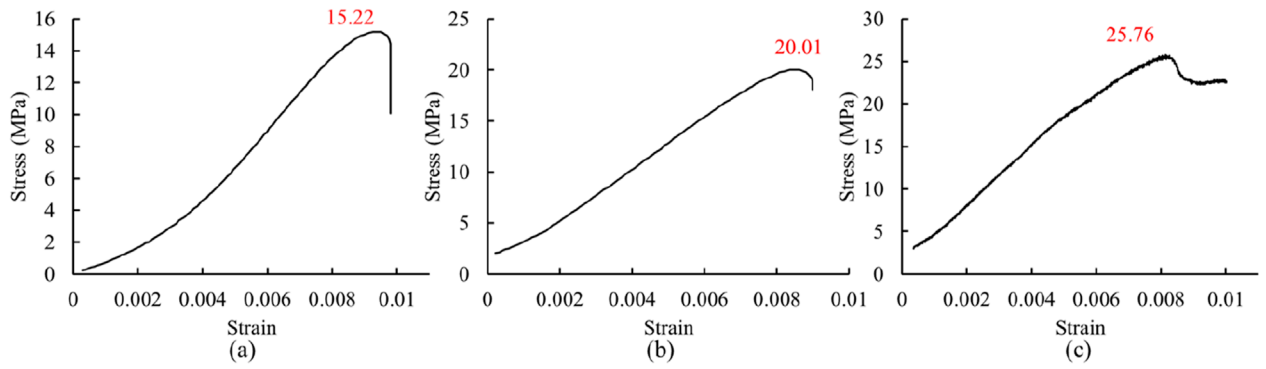

FIGURE 7
Stress-strain curve at a confining pressure of 2 MPa. **(A)** 1; **(B)** 2; **(C)** 3. The enrichment of natural cracks in coal rock samples leads to a high degree of difference in experimental results.

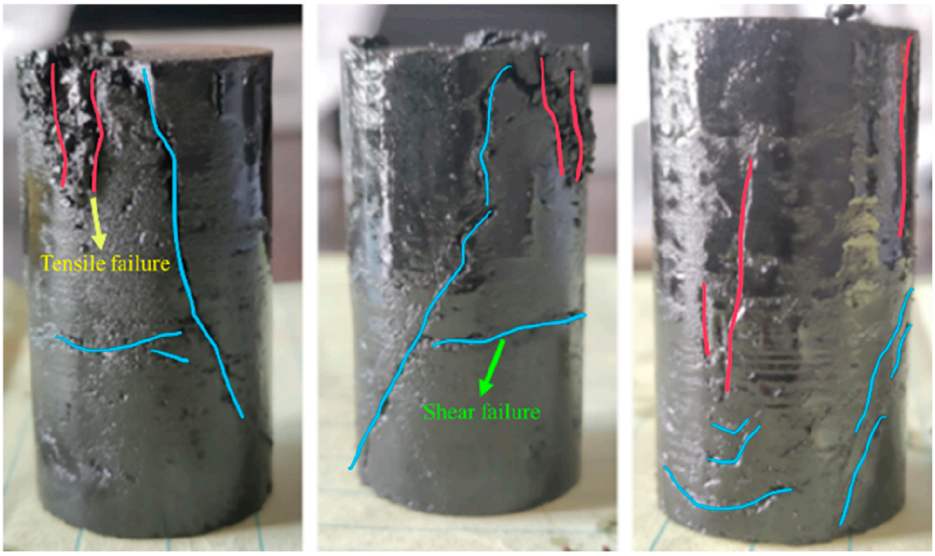

FIGURE 8
Schematic diagram of specimen failure form at confining pressure of 2 MPa (Blue shear failure, red tensile failure). Under the action of confining pressure, the fracture degree of coal rock samples is intensified, but the whole structure remains intact.

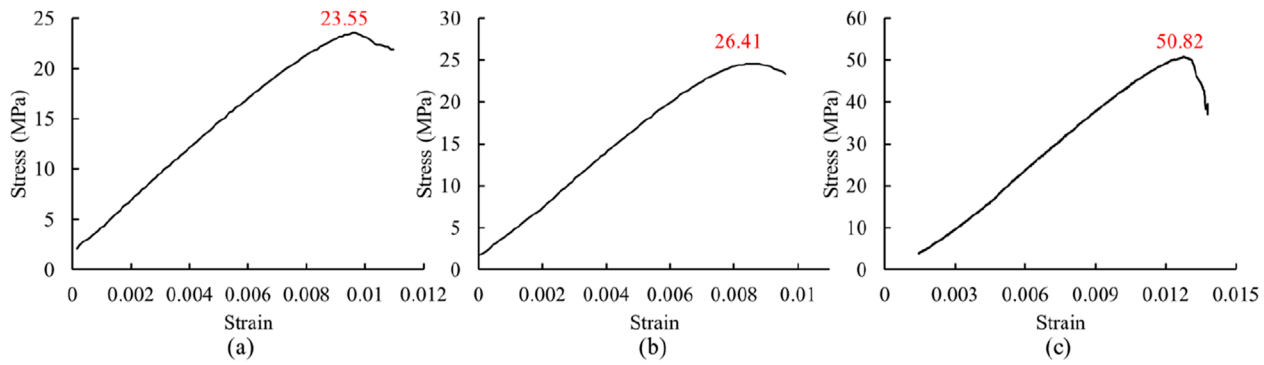

FIGURE 9
Stress-strain curve at a confining pressure of 4 MPa. **(A)** 1; **(B)** 2; **(C)** 3. The results of sample No. One and specimen No. 2 are similar, but the difference of specimen No. 3 is relatively high, which may be because there is no large number of natural cracks in specimen No. 3.

3.2.5 Situation in confining pressure of 8 MPa

When the confining pressure is increased to 8 MPa, the ultimate compressive strength of the specimen is also increased accordingly. The stress-strain curves of each specimen are shown in Figure 13, among which specimens one and two show more typical characteristics. However, the curve of specimen three fluctuates significantly, which indicates that the development of natural cracks in the specimen is relatively severe. In the triaxial compression test, these cracks are continuously compacted, which causes the stress of the specimen to fluctuate wildly. The failure mode of the specimen is shown in Figure 14. When the specimen is pressed, shear cracks are generated first, and then cracks extend tortuously along the surface of the specimen, resulting in a large number of cracks distributed on the surface of the specimen. Still, the specimen remains intact as a whole.

3.2.6 Situation in confining pressure of 10 MPa

When the confining pressure is increased to 10 MPa, the compressive strength of the three specimens in this group is all increased to 35 MPa, and the ultimate compressive strength of specimen one is further increased to 40 MPa, as shown in Figure 15. This result shows that the strength of coal rock rises with the increase of confining pressure. There are a few natural cracks in specimen 1; when the specimen is destroyed along these cracks, it still shows a particular residual strength. Therefore, the stress-strain curve of specimen one suddenly rises after falling, and secondary failure occurs. This indicates that the strength of coal rock specimens can still be affected by the natural cracks existing in the specimens under high confining pressure.

Under the compaction action of high confining pressure, the failure process of the test often becomes difficult, resulting in more complex failure forms of the specimen, as shown in Figure 16.

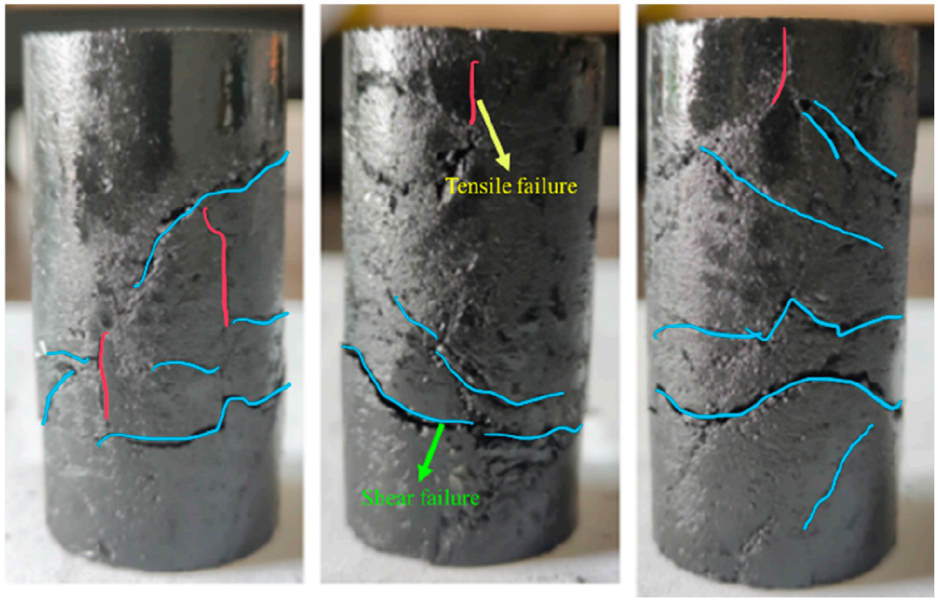

FIGURE 10
Schematic diagram of specimen failure form at confining pressure of 4 MPa (Blue shear failure, red tensile failure). A large number of shear cracks occurred after the specimen was broken, and the cracks mainly concentrated in the middle of the specimen.

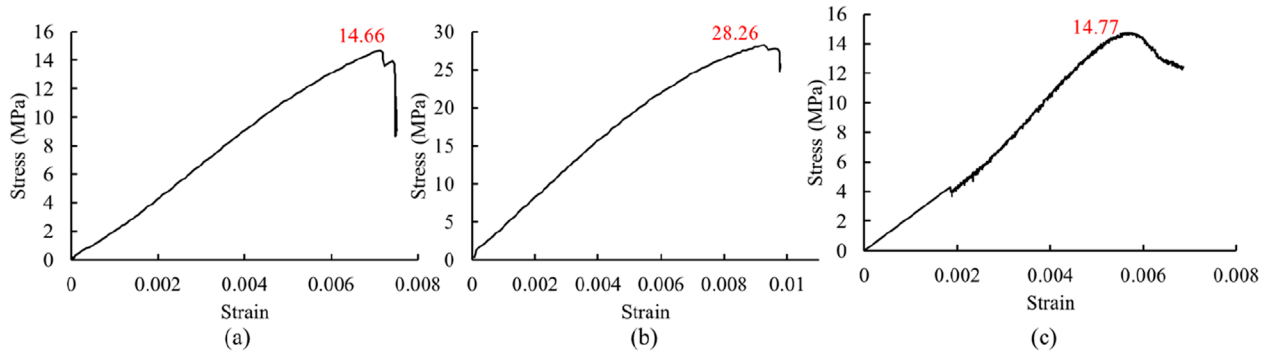

FIGURE 11
Stress-strain curve at confining pressure of 6 MPa; **(A)** 1; **(B)** 2; **(C)** 3. A large number of natural cracks cause the failure threshold of the sample to decrease significantly and the stress-strain curve to fluctuate significantly.

A macroscopic shear crack first appeared in the specimen, and the crack expanded rapidly, resulting in spalling on the specimen surface. Due to the confining pressure, the spalling part is still attached to the sample's surface during loading and participates in the pressure action until the sample is completely broken, so several horizontal cracks are generated in the middle of the coal rock.

After an in-depth study of coal-rock failure modes, we can divide them into three main types: tensile, shear, and mixed tension-shear failure. These failure modes reveal the different response modes of coal rock under stress and provide important clues to understanding the failure mechanism.

The above research shows that the natural random fissure in coal rock is one of the key factors affecting its failure form. These natural fractures make the coal rock samples show remarkable anisotropy characteristics, resulting in a highly uneven distribution of stress fields. This uneven stress distribution makes the fracture morphology complex and variable, greatly increasing the randomness of the basic mechanical parameters of the samples (Fu et al., 2021; Ji et al., 2015). Even the coal rock samples in the same area may show utterly different failure modes. At the same time, there is a significant correlation between the peak strength of coal and confining pressure. Under high confining pressure, coal rock usually shows strong bearing capacity and can effectively resist the action of external loads. However, in the process of coal seam mining, the strength of the coal seam wall in the working area will be greatly reduced due to the lack of confining pressure. This reduction in strength will increase the risk of wall collapse and seriously threaten mine safety production.

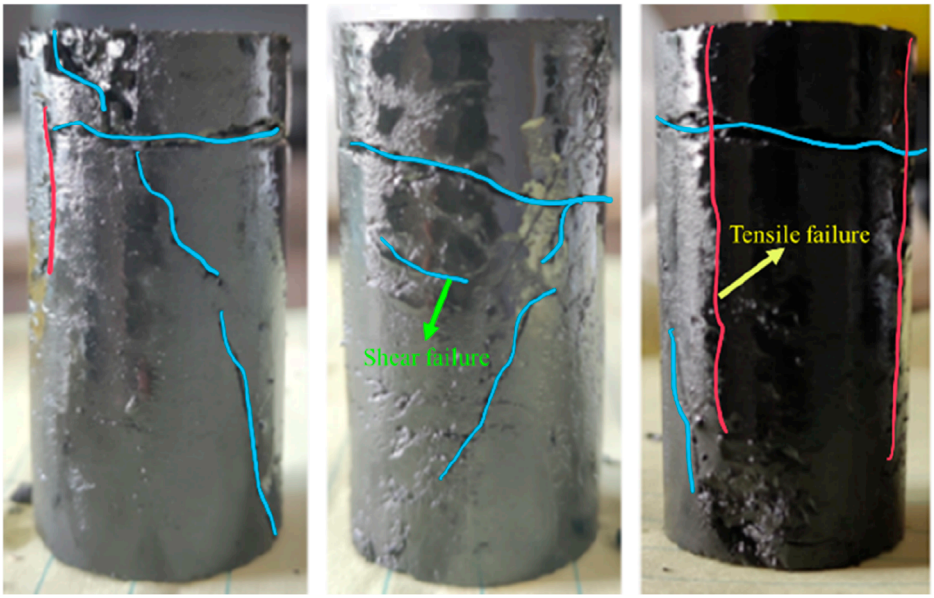

FIGURE 12
Schematic diagram of specimen failure form at confining pressure of 6 MPa (Blue shear failure, red tensile failure). Shear cracks, tension cracks, and natural cracks communicate with each other, resulting in sample failure.

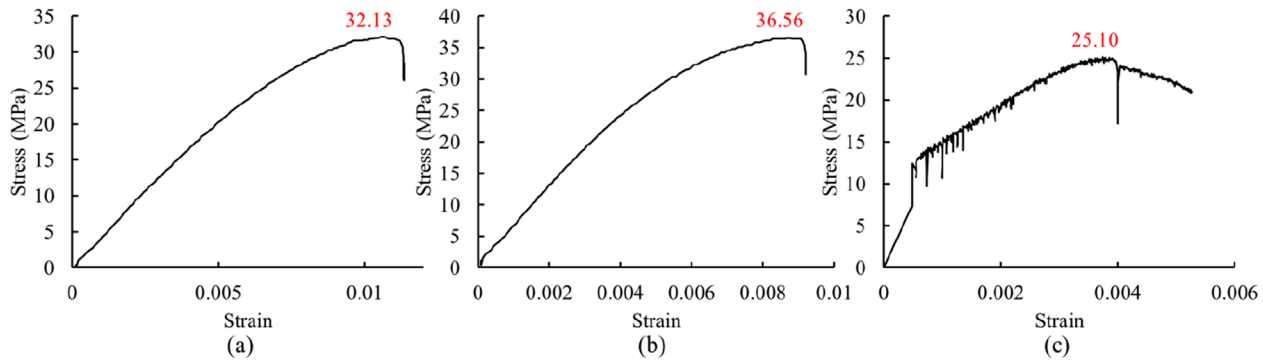

FIGURE 13
Stress-strain curve at confining pressure of 8 MPa: **(A)** 1; **(B)** 2; **(C)** 3. The stress-strain curves of specimens one and two show typical characteristics. The curve of specimen three fluctuates significantly, indicating that there are a large number of natural cracks in the specimen.

4 Gas migration law in mining fracture field

In the process of underground coal mining, with the continuous advancement of the coal mining face, the stress state of the coal rock in front of the workings changes, i.e., it causes stress release in the direction of the coal seam excavation and local stress concentration in the direction perpendicular to the coal seam excavation. When the stress state changes, the most direct effect is to cause deformation or destabilization of the coal rock layer, and the stress distribution is different at different locations. The deformation of the surrounding rock is also different, and the joints and fissures produced are different. After the deformation of the coal rock layer, the pore and fissure structure inside the coal rock layer changes, which makes the circulation channel of the gas in the coal rock layer change, leading to the change of the permeability of the gas in the coal rock layer, and greatly increasing the concentration of gas in the working face. Therefore, it is urgent to clarify the gas transportation law in the workplace, considering the collapse of coal rock and other factors. To this end, this section constructs the field mining fissure field morphology as shown in Figure 17 through the on-site data detection and test in Wangpo Mine and constructs the on-site gas transport model relying on COMSOL.

5 Numerical model

This model adopts a dual-medium structure of pores and cracks based on the special composition of coal. That is, coal is composed of pores, cracks, and matrix. In this structure, the matrix is divided

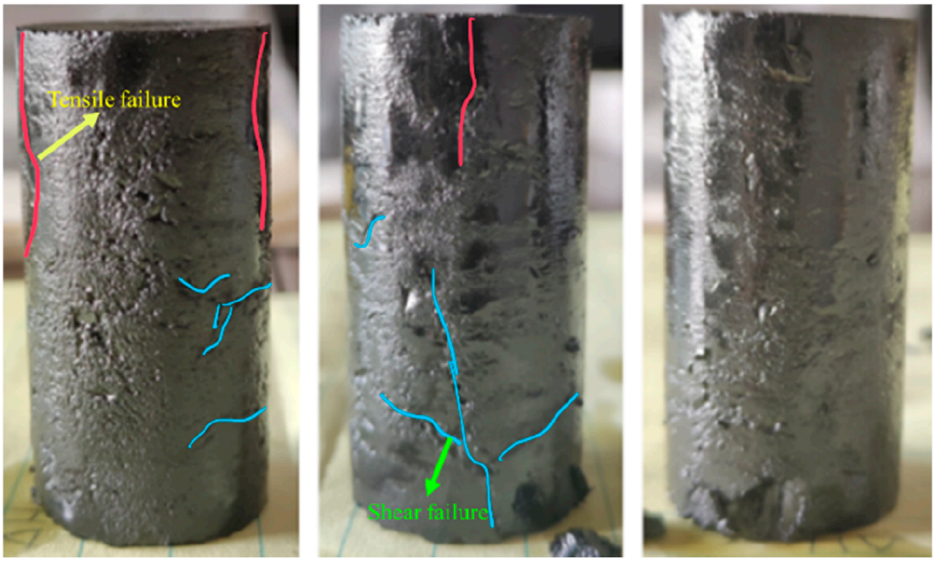

FIGURE 14
Schematic diagram of specimen failure form at confining pressure of 8 MPa (Blue shear failure, red tensile failure). The cracks of the sample were mainly concentrated at both ends of the sample, and the structure of the sample remained intact after the experiment.

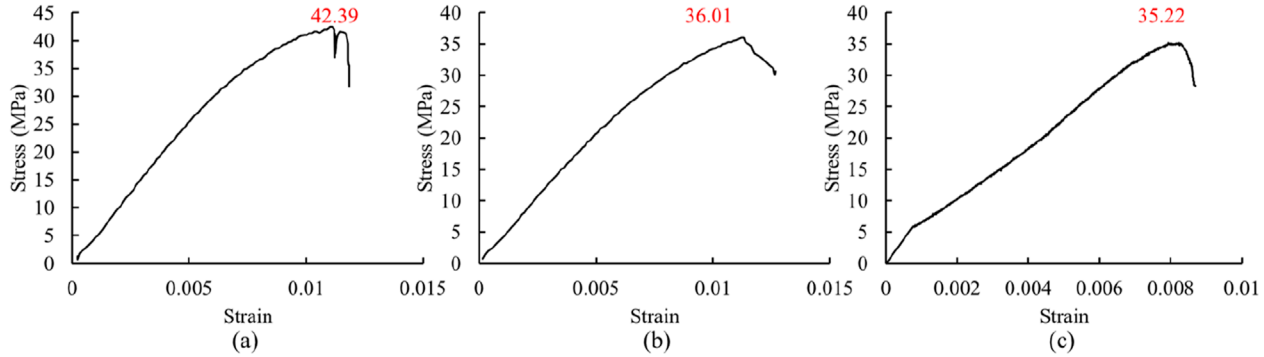

FIGURE 15
Stress-strain curve at confining pressure of 10 MPa. **(A)** 1; **(B)** 2; **(C)** 3. Under high confining pressure, even if the number of natural cracks in the specimen is different, the peak stress of the specimen has little change.

by cracks. Most of the gas exists in the matrix through adsorption, and its transport law follows Fick's diffusion law. However, a small part of gas exists in the fissure in a free state, and its migration law follows Darcy's seepage law.

In the ideal state without external interference, adsorbed and free gas maintain a dynamic balance. However, once this equilibrium state is broken, a continuous migration process will start, including diffusion and seepage, because the fracture's gas flow rate exceeds the matrix's diffusion rate. Specifically, the gas is first diffused from the matrix to the fissure utilizing Fick's diffusion law, driven by the difference in concentration. Subsequently, the gas will further migrate from the fissure to the borehole or roadway through Darcy seepage. The gas migration process of the coal seam is shown in Figure 18.

Considering the pore structure, gas migration form, and permeability characteristics of coal comprehensively, the pore structure characteristics and gas migration form of coal can be classified from a systematic perspective, including:

(1) Single pore - single permeability system: the pore structure of coal is idealized into a uniform fracture medium model, focusing on the permeability of the fracture. When the gas pressure balance in the coal seam is broken, the gas in the matrix can quickly desorb and diffuse into the fracture, and the gas migration process is mainly a single Darcy seepage form.
(2) Double-pore - single permeability system: the pore structure of coal is idealized into a dual medium model, including pores

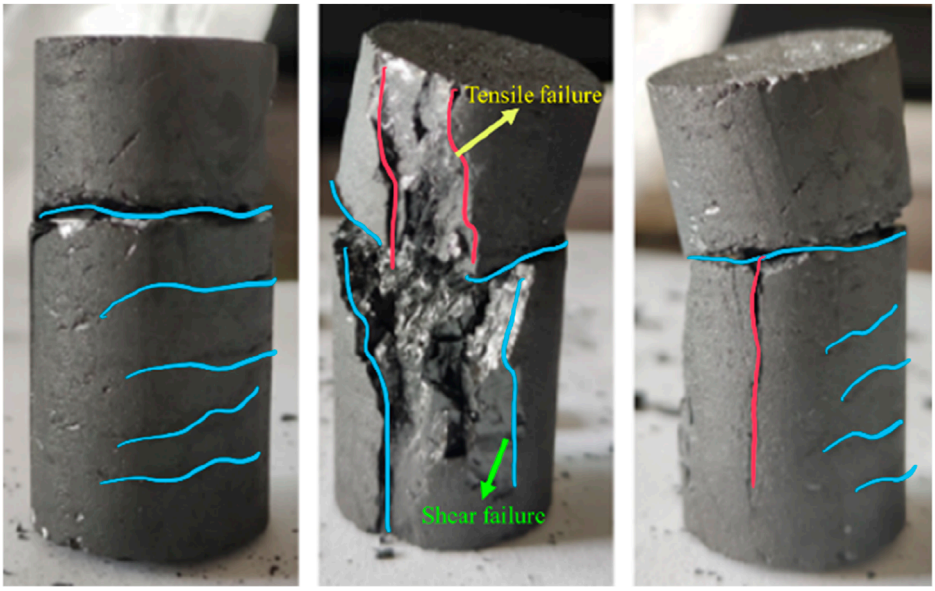

FIGURE 16
Schematic diagram of specimen failure form at confining pressure of 10 MPa (Blue shear failure, red tensile failure). It is difficult to destroy the sample under high confining pressure, and the degree of rupture after the experiment is high. The surface of the specimen is spalling, and several shear cracks run through the specimen.

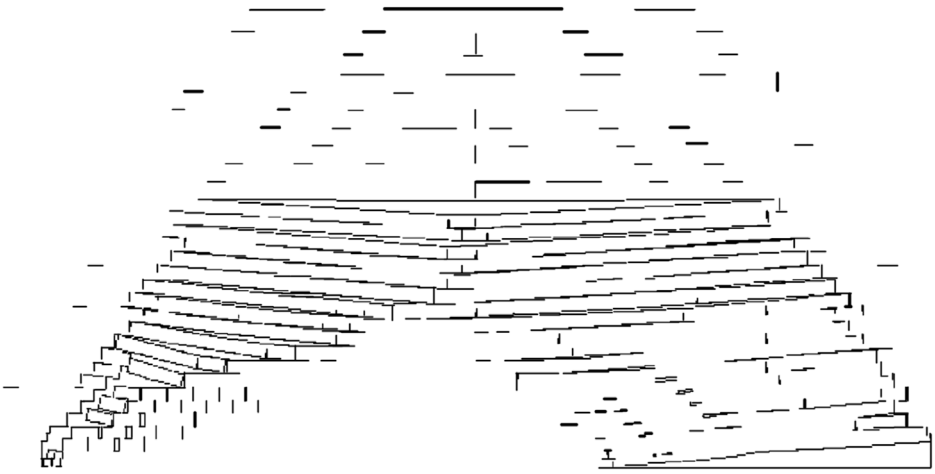

FIGURE 17
Fracture distribution in mining fracture field. The lines in the image represent cracks that have been created in the coal seam under mining disturbance.

and cracks, focusing on the permeability of cracks. In this case, gas migration in coal seams can be regarded as a two-step process in series.

(3) Double-pore - double-permeability system: the pore structure of coal is also idealized as a dual medium model including pores and cracks while considering the permeability of the matrix and cracks. Currently, gas migration in the coal seam can be regarded as a two-step process involving series and parallel connections. Specifically, the gas in the coal matrix not only enters the fracture in the form of diffusion but also migrates between the matrix in the form of seepage and finally enters the roadway or borehole.

5.1 Simplified treatment of gas-solid coupling between coal and gas

Due to the complex multi-field coupling solution of the model and the comprehensive impact of computational efficiency, the numerical simulation will be simplified as follows:

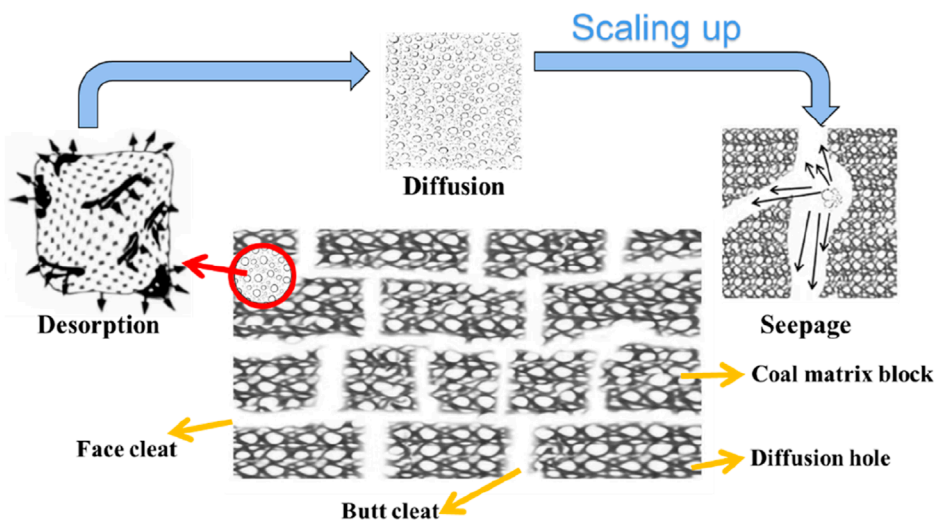

FIGURE 18
Schematic diagram of coal seam gas migration process. The gas first diffuses from the matrix to the fissure by means of Fick diffusion driven by the concentration difference. Subsequently, the gas will further migrate from the fissure to the borehole or roadway in the form of Darcy seepage.

(1) Suppose that the coal seam is a dry porous medium;
(2) The coal seam is a uniform and isotropic medium, and the influence of the anisotropy of the coal seam on the permeability directivity is ignored;
(3) The temperature in the gas flow field does not change much, and the gas migration in the coal seam is treated as an isothermal process;
(4) The coal seam fissures are filled with free gas, while the gas in the matrix exists in both adsorbed and free states;
(5) Gas is regarded as an ideal gas, and its dynamic viscosity remains unchanged under isothermal conditions;
(6) The pore and fissure systems are continuum systems.

5.2 Numerical simulation formula

(1) Gas occurrence quality per unit volume of coal

The free gas in the fracture system exists in the state of gas, and the mass of the free gas in the fracture system per unit volume of coal can be calculated by Equation 1:

$$m_f = \phi_f \rho_f \tag{1}$$

The m_f is the mass of free gas deposited per unit volume of coal, kg; ϕ_f is the fracture porosity of coal, %; ρ_f is the free gas density in the fracture system, kg/m^3.

The ideal gas equation of state is used to calculate the free gas density in the fracture system, and its expression is shown in Equation 2:

$$\rho_f = \frac{M_e}{RT} p_f \tag{2}$$

The M_e is the molar mass of methane, kg/mol; R is the ideal gas constant, J/(mol·K); T is the temperature of the coal seam, K; p_f is the gas pressure in the fracture system, MPa.

$$m_f \phi_f = \frac{M_e}{RT} p_f \tag{3}$$

In the coal matrix pore system, adsorbed and free gas exist, the main form of coal seam gas. The adsorbed gas conforms to Langmuir's adsorption equilibrium equation of state, whose expression is Equation 4:

$$m_{m1} = \frac{V_t p_m}{p_m + P_L} \rho_a \rho_s \tag{4}$$

The m_{m1} is the mass of adsorbed gas in the pore system of coal per unit volume, kg; V_t is the Langmuir volume, m^3; P_L is the Langmuir pressure, MPa; ρ_a is the mass of coal per unit apparent volume, kg/m^3; p_m is the gas pressure in matrix pores, MPa.

The density of gas in the standard state is calculated by Equation 5:

$$\rho_s = \frac{M_e}{V_m} \tag{5}$$

The V_m is the molar volume of methane in the standard state, m^3/mol. It can be calculated with Equation 6;

$$m_{m2} = \phi_m \frac{M_e}{RT} p_m \tag{6}$$

The m_{m2} is the occurrence mass of free gas in the pore system of coal per unit volume, kg; ϕ_m is the matrix porosity of the coal, %.

The total gas occurrence mass per unit volume of the coal matrix pore system is Equation 7:

$$m_m = \frac{V_t p_m}{p_m + P_L} \rho_a \frac{M_e}{V_M} + \phi_m \frac{M_e}{RT} p_m \tag{7}$$

The total gas occurrence mass per unit volume of coal is Equation 8:

$$m = \frac{V_t p_m}{p_m + P_L} \rho_a \frac{M_e}{V_M} + \phi_m \frac{M_e}{RT} p_m + \phi_f \frac{M_e}{RT} p_f \tag{8}$$

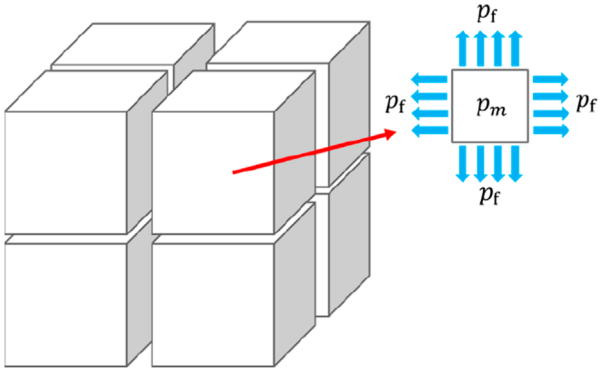

FIGURE 19
Mass exchange between matrix system and matrix system and matrix simplified model of matrix block.

(2) Control equation of gas diffusion in the coal matrix

Gas diffusion in a coal seam is mainly gas phase diffusion, as shown in Figure 19. The driving force of diffusion is the concentration difference between gaseous phase gas in the pores of the coal matrix and gas phase gas in cracks. In the process of gas extraction, the absorbed gas in the coal matrix as a mass source desorbs outward, making diffusion and seepage continue. The flux formula of mass exchange between the coal matrix and crack system can be expressed as is Equation 9:

$$Q_s = D\sigma_c\left(c_m - c_f\right) \tag{9}$$

The Q_s is the mass exchange rate between the coal matrix and fracture system per unit volume, kg/(mt ·s); D is the gas diffusion coefficient, m^2/s; σ_c is the matrix form factor, m^{-2}; c_m is the concentration of gas in the matrix, kg/m^3; c_f is the gas concentration in the fissure, kg/m^3.

The matrix shape factor σ_c is an essential parameter in the flux formula of mass exchange between the coal matrix and fracture system. For cubic type coal matrix, its form factor can be calculated as Equation 10:

$$\sigma_c = \frac{3\pi^2}{L^2} \tag{10}$$

L is the crack spacing, m.

Therefore, the governing equation of mass exchange between the coal matrix and fracture system can be expressed as Equation 11:

$$Q_s = \frac{\sigma_c DM}{RT}\left(p_m - p_f\right) \tag{11}$$

According to the gas migration characteristics in the extraction process, it can be seen that the matrix system is the positive mass source of the fissure system, and the fissure system is the negative mass source of the matrix system. Therefore, according to the law of conservation of mass, the mass exchange rate between the matrix system and the fissure system should be equal to the change of the mass of the matrix system with time, which can be expressed as Equation 12:

$$\frac{\partial m_m}{\partial_t} = -\frac{M}{\tau RT}\left(p_m - p_f\right) \tag{12}$$

The governing equation of matrix gas pressure change over time can be obtained by combining and simplifying as Equation 13:

$$\frac{\partial p_m}{\partial_t} = -\frac{V_m\left(p_m - p_f\right)\left(p_m + P_L\right)^2}{\tau V_L RTP_L\rho_a + \tau\phi_m V_M\left(p_m + P_L\right)^2} \tag{13}$$

(3) Control equation of seepage flow of fissure gas

Equation 14 is the mass conservation equation:

$$\frac{\partial\left(\phi_f\rho_f\right)}{\partial_t} = -V\left(\rho_f v\right) + Q_s\left(1 - \phi_f\right) \tag{14}$$

v is the gas seepage velocity in the fissure, m/s.

The gas in the fissure flows in the Darcy seepage mode, which can be calculated as Equation 15:

$$v = \frac{k_e}{\mu}\nabla p_f \tag{15}$$

k_e is the effective permeability of coal seam, Md; μ is the aerodynamic viscosity coefficient, Pa·S.

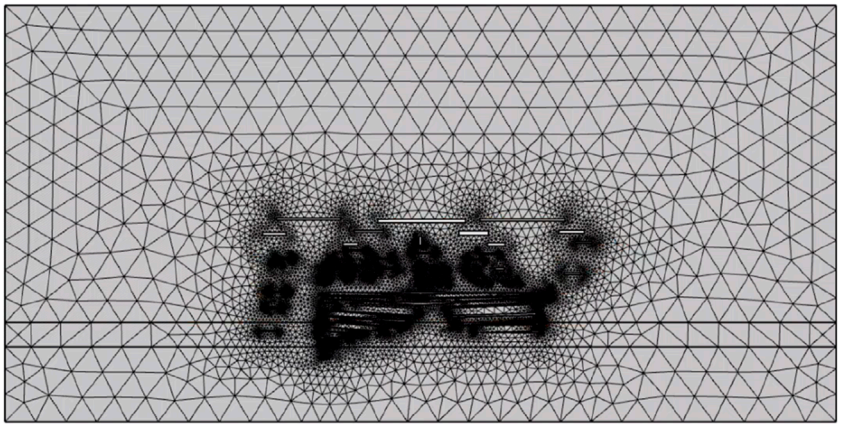

FIGURE 20
Grid division of mining-induced fracture field model. In order to improve the efficiency of calculation, the grid division of the crack area is finer.

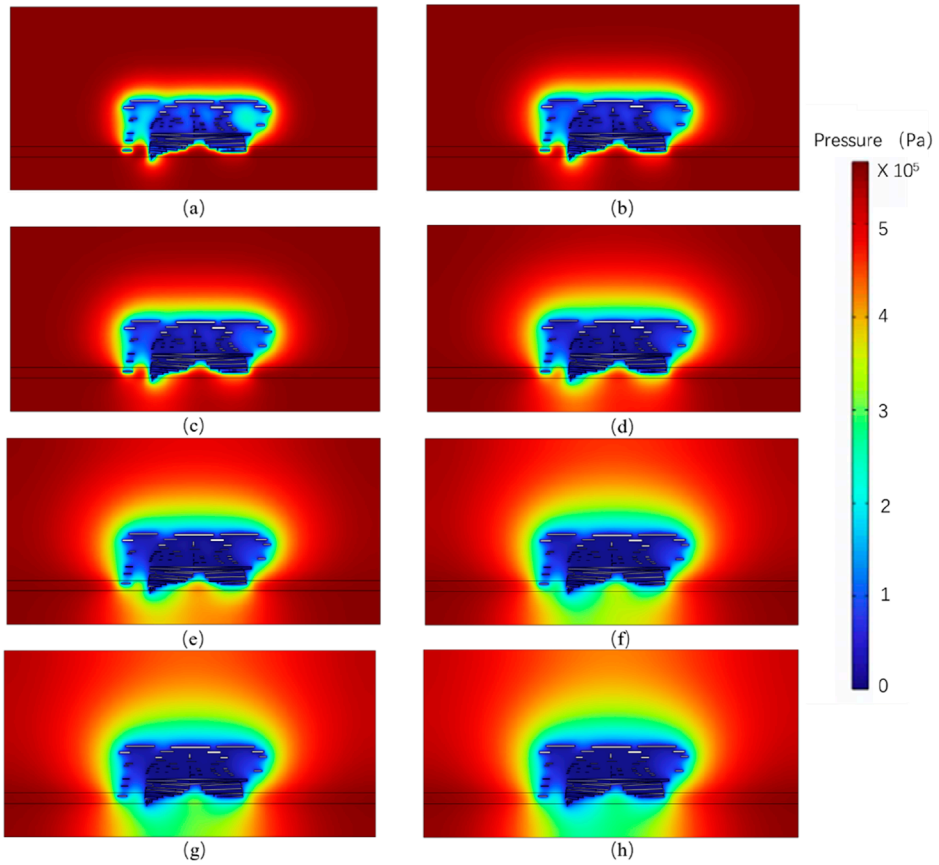

FIGURE 21
Gas migration cloud map. **(A)** 5; **(B)** 10; **(C)** 15; **(D)** 30; **(E)** 50; **(F)** 80; **(G)** 100; **(H)** 120. The color of the cloud image represents the gas pressure. In the first 100 days, the gas concentration decreased significantly with the increase in ventilation time. After 100 days of ventilation, the gas concentration hardly changed. In other words, 100 days of ventilation is the best ventilation time.

5.3 Result analysis

The collapse of the mining fracture field was imported into the COMSOL numerical simulation software, and its model was meshing. The meshing results are shown in Figure 20.

After the mesh division of the model is completed, the Dilliclet boundary condition is set. In the model, the crack surface is a natural crack under mining disturbance, and the condition is set as natural flow. Only the initial gas pressure is set in the upper and lower strata of the coal seam, and no additional gas is generated. Natural gas pressure and emission amount are set in the coal seam to investigate the law of gas migration under mining disturbance.

Coal seam gas dynamically evolves with time in the mining fracture field. Gas migration at different times is shown in Figure 21, and the color in the cloud map represents the gas pressure.

Due to the initial gas pressure in the overlying and lower strata in the model, the gas concentration and pressure in most areas were still high after 5 days of simulated natural ventilation. Only the gas migrated naturally at the crack area, and the gas concentration and pressure decreased, and the gas concentration in the center of the crack development area decreased significantly. With the increased natural ventilation time to 10 days, the gas concentration in the rock layer and coal seam close to the fracture area began to decrease. Because of the gas emission in the coal seam, the gas concentration near the coal seam was significantly higher.

After 30 days of ventilation, the gas concentration in the rock layer and coal seam around the crack is further reduced, and the low concentration range is relatively expanded, forming a low gas concentration area around the crack range. Under the influence of coal seam gas emission, the low concentration area is prominent in the upper part and small in the lower part. After 80 days of ventilation, the low-concentration area of gas increased significantly, and the concentration of coal seam near the fissure decreased significantly. This is because there is no gas pressure in the fissure itself, while there is gas pressure in the coal seam and its overlying and lower rock layers, resulting in gas migration toward the fissure. After 50 days of ventilation, most of the gas in the rock strata around the crack and the coal seam migrated along the crack, so the gas concentration in the coal seam close to the crack decreased significantly. When the ventilation time reaches 100 days, the gas concentration around the crack substantially reduces, and the gas

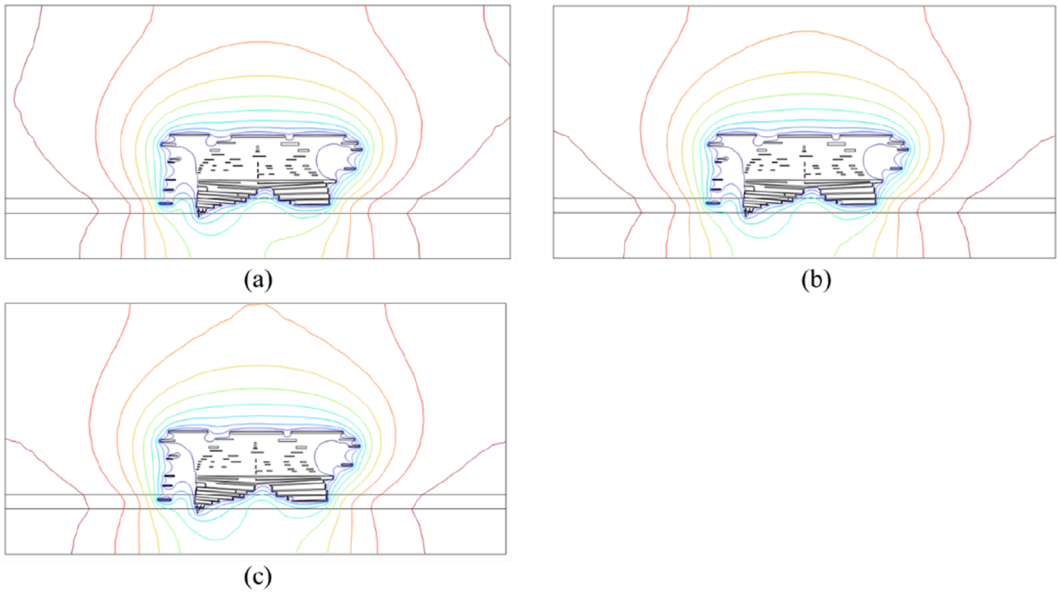

FIGURE 22
Gas pressure contours under different ventilation times. **(A)** 100; **(B)** 110; **(C)** 120. The gas pressure area does not change significantly after 100 days of ventilation and 110 days and 120 days of ventilation, so it is recommended to ventilate for at least 100 days.

pressure drops below 0.2 MPa. The gas concentration diagram after 120 days of ventilation has little change from that after 100 days of ventilation.

To explore the specific situation of coal seam gas migration in the mining fracture field with time change after 100, 110, and 120 days of ventilation, Figure 22 shows the contours of gas pressure under different ventilation times. The results show that the low gas pressure area does not change significantly after 100 days of ventilation and 110 days and 120 days of ventilation, so the recommended extraction time should be at least 100 days. In addition, compared with gas migration in the overlying rock matrix, the separation fractures and vertical fracture fractures in the mining fracture field have gas flow orientation.

The evolution law of gas pressure at different positions in coal seams with ventilation time is still the focus of attention. Therefore, 11 detection points are set in this paper, as shown in Figure 23A. The total length of each point is 100m, and all of them are areas where gas concentration changes significantly after long-term ventilation.

Figure 23B shows the variation curve of gas pressure at each point. With the increase of time, the gas pressure at each point decreases in different amplitude. The closer to the crack, the more pronounced the decreasing trend of gas pressure is. So, in the leftmost detection point (50,20) and the two rightmost detection points (140,20; 150,20), the pressure drop trend is the weakest, the fourth detection point on the left (80,20) is closest to the fracture, and the gas pressure drop is the most significant. In addition, after the gas migration time reaches 100 days, the gas pressure curve at each point is stable, which also shows that after the ventilation time reaches 100 days, the gas migration speed and low gas area change little.

Therefore, with gas migration in the mining fracture field, the gas enrichment area is located in the coal seam area far away from the mining fracture.

6 Conclusion

This work employs uniaxial and triaxial compression experiments to investigate the failure process of fractured coal rock. Using the data collected from the field survey, a model is developed to transport coal seam gas in the mining fracture field. This model also defines the behavior of coal seam gas transport when subjected to stress disturbances. The primary findings can be summarized as follows:

(1) Coal rock exhibits three common failure modes: tensile failure, shear failure, and a combination of tension and shear failure. The stochastic arrangement of natural cracks in coal rock is the primary determinant that renders the anticipation of fracture failure mode challenging. Additionally, it is the primary factor contributing to the significant variation in the mechanical durability of coal rock within a given area.
(2) The peak strength of coal rock is significantly correlated with confining pressure. Under high confining pressure, coal rock typically exhibits strong bearing capacity.
(3) An analysis was conducted on the dynamic evolution law of gas migration at different times. It was observed that in the overlaying strata area of the mining fracture field, the gas pressure was initially higher and reduced significantly as time progressed. Compared with the overlying rock matrix

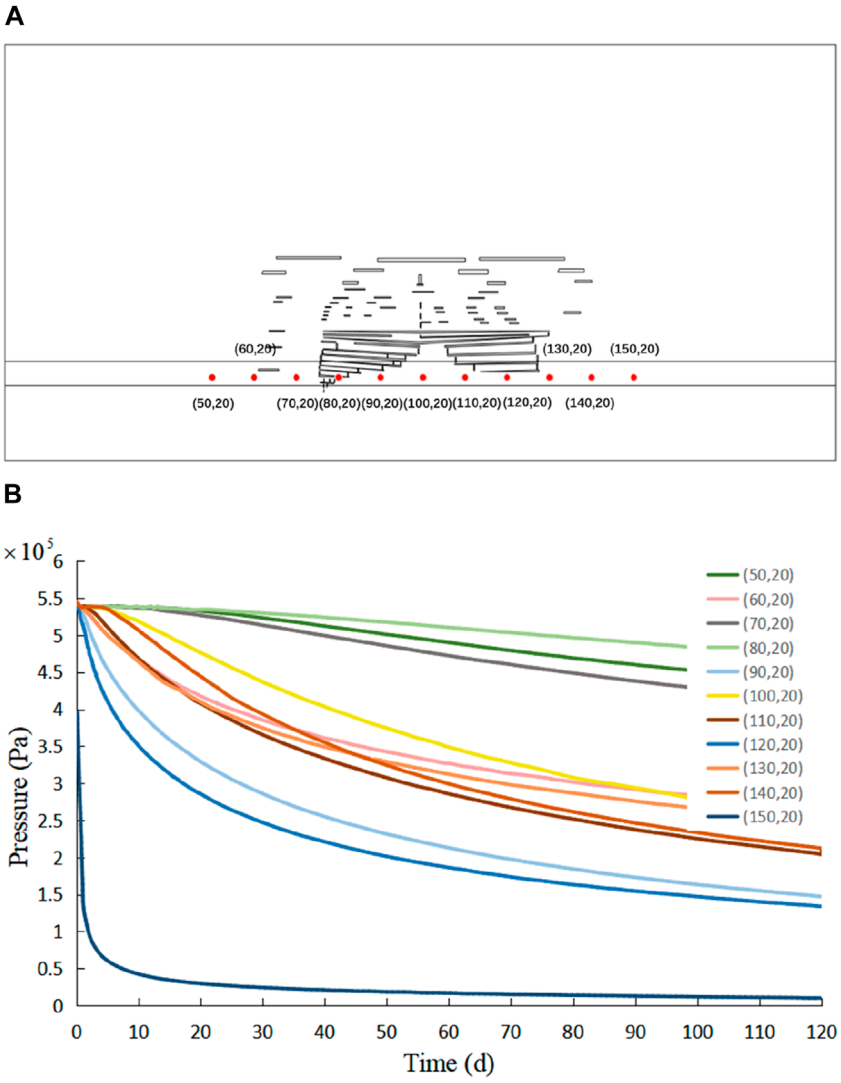

FIGURE 23
Monitoring points and monitoring curves. **(A)** Schematic diagram of points 1 to 11; **(B)** Gas migration curve from points 1 to 11. A total of 11 detection points were set up to detect the evolution law of gas pressure at different positions in coal seams with ventilation time. The total length is 100 m, and each point is 10 m apart. With the increase of time, the gas pressure at each point has a different amplitude of decline, and the closer to the crack, the more obvious the gas pressure decline trend. In addition, when the gas migration time reaches 100 days, the gas pressure curve at each point is basically stable.

migration, the separation and vertical fracture fractures in the mining fracture field have gas flow orientation. With the movement of gas in the trapezoidal stage of the mining fracture field, the gas enrichment area is located in the coal seam area far away from the mining fracture.

(4) The simulation results of gas migration under mining disturbance show that the low gas pressure area changes little after 100 days of ventilation. Therefore, to ensure project safety, the ventilation time of a fully mechanized mining face should reach at least 100 days.

Data availability statement

The raw data supporting the conclusions of this article will be made available by the authors, without undue reservation.

Author contributions

FD: Methodology, Writing–original draft. BL: Formal Analysis, Software, Writing–original draft. YR: Investigation, Methodology, Writing–original draft. XL: Data curation, Writing–review and editing. LP: Data curation, Software, Writing–review and editing. ZF: Formal Analysis, Methodology, Writing–review and editing. WL: Data curation, Writing–review and editing.

Funding

The author(s) declare that financial support was received for the research, authorship, and/or publication of this article. The authors acknowledge the support provided by the Natural Science Starting Project of SWPU (Gran No. 2022QHZ009).

Conflict of interest

Author WL was employed by PetroChina Southwest Oil & Gasfield Company.

The remaining authors declare that the research was conducted in the absence of any commercial or financial relationships that could be construed as a potential conflict of interest.

Publisher's note

References

Alexeev, A. D., Feldman, E. P., and Vasilenko, T. A. (2007). Methane desorption from a coal-bed. *Fuel* 86 (16), 2574–2580. doi:10.1016/j.fuel.2007.02.005

Chai, Y., Dou, L., Cai, W., Małkowski, P., Li, X., Gong, S., et al. (2023). Experimental investigation into damage and failure process of coal-rock composite structures with different roof lithologies under mining-induced stress loading. *Int. J. Rock Mech. Min. Sci.* 170, 105479. doi:10.1016/j.ijrmms.2023.105479

Chen, H., Liu, K., Shi, T., and Wang, L. (2022a). Coal consumption and economic growth: a Chinese city-level study. *Energy Econ.* 109, 105940. doi:10.1016/j.eneco.2022.105940

Chen, H., Liu, K., Shi, T., and Wang, L. (2022c). Coal consumption and economic growth: a Chinese city-level study. *Energy Econ.* 109, 105940. doi:10.1016/j.eneco.2022.105940

Chen, J., Li, Z., Song, M., Wang, Y., Wu, Y., and Li, K. (2022b). Economic and intensity effects of coal consumption in China. *J. Environ. Manag.* 301, 113912. doi:10.1016/j.jenvman.2021.113912

Chen, W., and Xu, R. (2010). Clean coal technology development in China. *Energy policy* 38 (5), 2123–2130. doi:10.1016/j.enpol.2009.06.003

Cheng, Z., Liu, B., Zou, Q., Wang, X., Feng, J., Zhao, Z., et al. (2020). Analysis of spatial–temporal evolution of mining-induced fracture field: a case study using image processing in the Shaqu Coal Mine, China. *Nat. Resour. Res.* 29, 1601–1615. doi:10.1007/s11053-019-09540-2

Chi, P., Sun, J., Yan, W., and Luo, X. (2024). Multiscale fusion of tight sandstone digital rocks using attention-guided generative adversarial network. *Mar. Petroleum Geol.* 160, 106647. doi:10.1016/j.marpetgeo.2023.106647

Cui, R., Sun, J., Liu, H., Dong, H., and Yan, W. (2024). Pore structure and gas adsorption characteristics in stress-loaded shale on molecular simulation. *Energy* 286, 129658. doi:10.1016/j.energy.2023.129658

Cui, X., and Bustin, R. M. (2005). Volumetric strain associated with methane desorption and its impact on coalbed gas production from deep coal seams. *Aapg Bull.* 89 (9), 1181–1202. doi:10.1306/05110504114

Fu, G., Xie, X., Jia, Q., Tong, W., and Ge, Y. (2020). Accidents analysis and prevention of coal and gas outburst: understanding human errors in accidents. *Process Saf. Environ. Prot.* 134, 1–23. doi:10.1016/j.psep.2019.11.026

Fu, H., Huang, L., Zhang, F., Xu, Y., Cai, B., and Liang, T. (2021). Effect of perforation technologies on the initiation and propagation of hydraulic fracture. *Chin. J. Rock Mech. Eng.* 40, 3163–3173. doi:10.13722/j.cnki.jrme.2021.0573

Fu, H., Huang, L., Hou, B., Weng, D., Guan, B., Zhong, T., et al. (2024). Experimental and numerical investigation on interaction mechanism between hydraulic fracture and natural fracture. *Rock Mech. Rock Eng.* doi:10.1007/s00603-024-04101-3

Gan, Y., Wu, S., Niu, D., and Liang, W. (2024). Multimechanism of gas transportation in micro–nanoscale pores of coal seam: an advanced model of gas adsorption and diffusion. *Energy and Fuels* 38, 7899–7916. doi:10.1021/acs.energyfuels.4c00785

Gao, J., Li, X., Cheng, G., Luo, H., and Zhu, H. (2023). Structural evolution and characterization of organic-rich shale from macroscopic to microscopic resolution: the significance of tectonic activity. *Adv. Geo-Energy Res.* 10 (2), 84–90. doi:10.46690/ager.2023.11.03

He, R., Yang, J., Li, L., Yang, Z., Chen, W., Zeng, J., et al. (2023). Investigating the simultaneous fracture propagation from multiple perforation clusters in horizontal wells using 3D block discrete element method. *Front. Earth Sci.* 11, 1115054. doi:10.3389/feart.2023.1115054

Huang, L., Dontsov, E., Fu, H., Lei, Y., Weng, D., and Zhang, F. (2022). Hydraulic fracture height growth in layered rocks: perspective from DEM simulation of different propagation regimes. *Int. J. Solids Struct.* 238, 111395. doi:10.1016/j.ijsolstr.2021.111395

Huang, L., He, R., Yang, Z., Tan, P., Chen, W., Li, X., et al. (2023a). Exploring hydraulic fracture behavior in glutenite formation with strong heterogeneity and variable lithology based on DEM simulation. *Eng. Fract. Mech.* 278, 109020. doi:10.1016/j.engfracmech.2022.109020

Huang, L., Liao, X., Fan, M., Wu, S., Tan, P., and Yang, L. (2024). Experimental and numerical simulation technique for hydraulic fracturing of shale formations. *Adv. Geo-Energy Res.* 13 (2), 83–88. doi:10.46690/ager.2024.08.02

Huang, L., Liu, J., Zhang, F., Dontsov, E., and Damjanac, B. (2019). Exploring the influence of rock inherent heterogeneity and grain size on hydraulic fracturing using discrete element modeling. *Int. J. Solids Struct.* 176, 207–220. doi:10.1016/j.ijsolstr.2019.06.018

Huang, L., Liu, J., Zhang, F., Fu, H., Zhu, H., and Damjanac, B. (2020). 3D lattice modeling of hydraulic fracture initiation and near-wellbore propagation for different perforation models. *J. Petroleum Sci. Eng.* 191, 107169. doi:10.1016/j.petrol.2020.107169

Huang, L., Tan, J., Fu, H., Liu, J., Chen, X., Liao, X., et al. (2023b). The non-plane initiation and propagation mechanism of multiple hydraulic fractures in tight reservoirs considering stress shadow effects. *Eng. Fract. Mech.* 292, 109570. doi:10.1016/j.engfracmech.2023.109570

Ji, Y., Wang, J., and Zhang, L. (2015). Analysis on inflowing of the injecting water in faulted formation. *Adv. Mech. Eng.* 7 (6), 1687814015590294–2076. doi:10.1007/s00603-019-02042-w

Jia, L., Peng, S., Xu, J., and Yan, F. (2022). Experimental investigation on disturbance effect during coalbed methane production. *J. Petroleum Sci. Eng.* 208, 109591. doi:10.1016/j.petrol.2021.109591

Jia, Z., Xie, H., Zhang, R., Li, C., Wang, M., Gao, M., et al. (2020). Acoustic emission characteristics and damage evolution of coal at different depths under triaxial compression. *Rock Mech. Rock Eng.* 53, 2063–2076. doi:10.1007/s00603-019-02042-w

Jiang, Y., Liang, B., Wang, D., Luan, H., Zhang, G., Dong, L., et al. (2024). Experimental study on failure mechanical properties and acoustic emission characteristics of soft rock–coal combination under dynamic disturbance. *Eng. Fail. Anal.* 158, 108016. doi:10.1016/j.engfailanal.2024.108016

Kong, D. Z., Cheng, Z. B., and Zheng, S. S. (2019). Study on the failure mechanism and stability control measures in a large-cutting-height coal mining face with a deep-buried seam. *Bull. Eng. Geol. Environ.* 78, 6143–6157. doi:10.1007/s10064-019-01523-0

Kuang, N., Zhou, J., Xian, X., Zhang, C. p., Yang, K., and Dong, Z. q. (2023). Geomechanical risk and mechanism analysis of CO2 sequestration in unconventional coal seams and shale gas reservoirs. *Rock Mech. Bull.* 2 (4), 100079. doi:10.1016/j.rockmb.2023.100079

Li, D., Wu, D., Xu, F., Lai, J., and Shao, L. (2018a). Literature overview of Chinese research in the field of better coal utilization. *J. Clean. Prod.* 185, 959–980. doi:10.1016/j.jclepro.2018.02.216

Li, J., and Hu, S. (2017). History and future of the coal and coal chemical industry in China. *Resour. Conservation Recycl.* 124, 13–24. doi:10.1016/j.resconrec.2017.03.006

Li, S., Gao, M., Yang, X., Zhang, R., Ren, L., Zhang, Z., et al. (2018b). Numerical simulation of spatial distributions of mining-induced stress and fracture fields for three coal mining layouts. *J. Rock Mech. Geotechnical Eng.* 10 (5), 907–913. doi:10.1016/j.jrmge.2018.02.008

Li, Y., Pan, S., Ning, S., Shao, L., Jing, Z., and Wang, Z. (2022a). Coal measure metallogeny: metallogenic system and implication for resource and environment. *Sci. China Earth Sci.* 65 (7), 1211–1228. doi:10.1007/s11430-021-9920-4

Liang, T., Liu, X., Wang, S., Wang, E., and Li, Q. (2018). Study on the fractal characteristics of fracture network evolution induced by mining. *Adv. Civ. Eng.* 2018, 2018. doi:10.1155/2018/9589364

Liu, C., Yu, B., Zhao, H., Hong, Z., Tian, Z., Zhang, D., et al. (2022c). Effective stress effect and slippage effect of gas migration in deep coal reservoirs. *Int. J. Rock Mech. Min. Sci.* 155, 105142. doi:10.1016/j.ijrmms.2022.105142

Liu, T., Xu, D., Shi, L., Qu, L., and Ji, K. (2022b). Trapezoidal collapse model to calculate the height of the overburden collapse zone in coal seam mining: an example from Guo'Jiahe Coal Mine, Western China. *Energy* 256, 124609. doi:10.1016/j.energy.2022.124609

Liu, T., Zhao, Y., Kong, X., Lin, B., and Zou, Q. (2022a). Dynamics of coalbed methane emission from coal cores under various stress paths and its application

in gas extraction in mining-disturbed coal seam. *J. Nat. Gas Sci. Eng.* 104, 104677. doi:10.1016/j.jngse.2022.104677

Luo, H., Xie, J., Huang, L., Wu, J., Shi, X., Bai, Y., et al. (2022). Multiscale sensitivity analysis of hydraulic fracturing parameters based on dimensionless analysis method. *Lithosphere* 2022 (Special 12), 9708300. doi:10.2113/2022/9708300

Qin, Y., Xu, H., Liu, W., Liu, J., and Duan, W. (2020). Time-and pressure-independent gas transport behavior in a coal matrix: model development and improvement. *Energy and Fuels* 34 (8), 9355–9370. doi:10.1021/acs.energyfuels.0c01182

Saber, E., Qu, Q., Aminossadati, S. M., Zhu, Y., and Chen, Z. (2024). Horizontal borehole azimuth optimization for enhanced stability and coal seam gas production. *Rock Mech. Bull.* 3 (1), 100100. doi:10.1016/j.rockmb.2023.100100

Shu, L., Wang, K., Liu, Z., Zhao, W., Zhu, N., and Lei, Y. (2022). A novel physical model of coal and gas outbursts mechanism: insights into the process and initiation criterion of outbursts. *Fuel* 323, 124305. doi:10.1016/j.fuel.2022.124305

Song, H., Duan, C., Zhao, Y., Teng, T., Hu, S., Wu, Y., et al. (2024). Effect of cyclic loading-unloading on the mechanical anisotropy of coal under uniaxial compressive condition. *Bull. Eng. Geol. Environ.* 83 (4), 131. doi:10.1007/s10064-024-03631-y

Tan, P., Chen, Z., Huang, L., Zhao, Q., and Shao, S. (2024a). Evaluation of the combined influence of geological layer property and in-situ stresses on fracture height growth for layered formations. *Pet Sci.*, 1995–8226. doi:10.1016/j.petsci.2024.07.014

Tan, P., Fu, S., Huang, L., Chen, Z., and Cao, J. (2024b). Effects of orthogonal cleat structures on hydraulic fracture evolution behavior. *Geoenergy Sci. Eng.* 213119, 2949–8910. doi:10.1016/j.geoen.2024.213119

Tao, M., Cheng, W., Nie, K., Zhang, X., and Cao, W. (2022). Life cycle assessment of underground coal mining in China. *Sci. total Environ.* 805, 150231. doi:10.1016/j.scitotenv.2021.150231

Tian, C., Liu, Y., Yang, X., Hu, Q., Wang, B., and Yang, H. (2020). Development characteristics and field detection of overburden fracture zone in multiseam mining: a case study. *Energy Sci. and Eng.* 8 (3), 602–615. doi:10.1002/ese3.536

Wang, F., Ren, T., Tu, S., Hungerford, F., and Aziz, N. (2012). Implementation of underground longhole directional drilling technology for greenhouse gas mitigation in Chinese coal mines. *Int. J. Greenh. Gas Control* 11, 290–303. doi:10.1016/j.ijggc.2012.09.006

Wang, J., and Cao, H. (2022). Improving competitive strategic decisions of Chinese coal companies toward green transformation: a hybrid multi-criteria decision-making model. *Resour. Policy* 75, 102483. doi:10.1016/j.resourpol.2021.102483

Wang, J., Feng, L., Davidsson, S., and Höök, M. (2013). Chinese coal supply and future production outlooks. *Energy* 60, 204–214. doi:10.1016/j.energy.2013.07.031

Wang, K., Wang, Y., Xu, C., Guo, H., Xu, Z., Liu, Y., et al. (2023). Modeling of multi-field gas desorption-diffusion in coal: a new insight into the bidisperse model. *Energy* 267, 126534. doi:10.1016/j.energy.2022.126534

Wang, L., Lu, Z., Chen, D., Liu, Q. q., Chu, P., Shu, L. y., et al. (2020). Safe strategy for coal and gas outburst prevention in deep-and-thick coal seams using a soft rock protective layer mining. *Saf. Sci.* 129, 104800. doi:10.1016/j.ssci.2020.104800

Xiong, Y., Kong, D., Wen, Z., Wu, G., and Liu, Q. (2022). Analysis of coal face stability of lower coal seam under repeated mining in close coal seams group. *Sci. Rep.* 12 (1), 509. doi:10.1038/s41598-021-04410-5

Yang, Y., Li, X., He, W., and Zhang, B. (2023b). Comparative analysis of deformation failure and energy properties of raw coal and sandstone under uniaxial compression. *J. Petroleum Explor. Prod. Technol.* 13 (2), 543–552. doi:10.1007/s13202-022-01573-3

Yang, Y., Li, Y., Wang, L., and Wu, Y. (2023a). On strata damage and stress disturbance induced by coal mining based on physical similarity simulation experiments. *Sci. Rep.* 13 (1), 15458. doi:10.1038/s41598-023-42148-4

Yuan, J. (2018). The future of coal in China. *Resour. Conservation Recycl.* 129, 290–292. doi:10.1016/j.resconrec.2016.12.006

Zeng, F., Peng, F., Guo, J., Wang, D., Zhang, S., Zhang, P., et al. (2019). Gas transport study in the confined microfractures of coal reservoirs. *J. Nat. Gas Sci. Eng.* 68, 102920. doi:10.1016/j.jngse.2019.102920

Zhang, B., Li, X., and Zhang, D. (2021). Study on mechanical and permeability characteristics of containing gas coal-rock under conventional triaxial compression. *Geotechnical Geol. Eng.* 39 (8), 5775–5786. doi:10.1007/s10706-021-01866-0

Zhang, C., Chen, Y., Ren, Z., and Wang, F. (2024). Compaction and seepage characteristics of broken coal and rock masses in coal mining: a review in laboratory tests. *Rock Mech. Bull.* 3, 100102. doi:10.1016/j.rockmb.2024.100102

Zhang, F., Huang, L., Yang, L., Dontsov, E., Weng, D. W., Liang, H. B., et al. (2022a). Numerical investigation on the effect of depletion-induced stress reorientation on infill well hydraulic fracture propagation. *Petroleum Sci.* 19 (1), 296–308. doi:10.1016/j.petsci.2021.09.014

Zhang, Q., Wang, Z., Zhang, J., Jiang, H., Wang, Y., Yang, K., et al. (2022b). Integrated green mining technology of "coal mining-gangue washing-backfilling-strata control-system monitoring"—taking Tangshan Mine as a case study. *Environ. Sci. Pollut. Res.* 29 (4), 5798–5811. doi:10.1007/s11356-021-16083-8

Zheng, Y., He, R., Huang, L., Bai, Y., Wang, C., Chen, W., et al. (2022). Exploring the effect of engineering parameters on the penetration of hydraulic fractures through bedding planes in different propagation regimes. *Comput. Geotechnics* 146, 104736. doi:10.1016/j.compgeo.2022.104736

Zhou, J., Wang, X., Collett, T. S., Li, S., Kuang, Z., Lu, Y., et al. (2023). Characterization of a complex sand-rich gas hydrate reservoir system in the Indian marine continental margin with downhole log and seismic data. *Mar. Petroleum Geol.* 155, 106370. doi:10.1016/j.marpetgeo.2023.106370

Zhu, H., Huang, C., Ju, Y., Bu, H., Li, X., Yang, M., et al. (2021). Multi-scale multi-dimensional characterization of clay-hosted pore networks of shale using FIBSEM, TEM, and X-ray micro-tomography: implications for methane storage and migration. *Appl. Clay Sci.* 213, 106239. doi:10.1016/j.clay.2021.106239

Zhu, H., Ju, Y., Qi, Y., Huang, C., and Zhang, L. (2018). Impact of tectonism on pore type and pore structure evolution in organic-rich shale: implications for gas storage and migration pathways in naturally deformed rocks. *Fuel* 228, 272–289. doi:10.1016/j.fuel.2018.04.137